Title

Competing Intermolecular and Molecule—Surface Interactions: Dipole—Dipole-Driven Patterns in Mixed Carborane Self-Assembled Monolayers

Authors

White, Katherine E

Avery, Erin M

Cummings, Edison

et al.

Isomeric Molecules Mapping within Mixed Carborane SAMs: Revealing Dipole-Dipole Driven Patterns

Katherine White,[1,2] Erin Avery,[1,2] Edison Cummings,[1] Zixiang Hong,[1] Jens Langecker,[3]

Aliaksei Vetushka,[4] Michal Dusek,[4] Jan Machacek,[3] Jakub Visnak,[3,5] Jan Endres,[6]

Zdenek Bastl,[7] Ersen Mete,[8*] Anastassia N. Alexandrova,[1,2,10*] Tomas Base,[1,2,3*] and

Paul S. Weiss[1,2,9,10*]

[1]Department of Chemistry and Biochemistry, University of California, Los Angeles, Los Angeles, California 90095, United States

[2]California NanoSystems Institute, University of California, Los Angeles, Los Angeles, California 90095, United States

[3]The Czech Academy of Sciences, Institute of Inorganic Chemistry, 250 68 Husinec-Rez, c.p. 1001, Czech Republic

[4]The Czech Academy of Sciences, Institute of Physics, Na Slovance 1999/2, 182 21 Prague 8,
Czech Republic

[5]Department of Chemistry, Middle East Technical University, Ankara 06800, Turkiye

[6]Department of Condensed Matter Physics, Faculty of Mathematics and Physics, Charles University, Ke Karlovu 2026/5, 121 16 Praha 2, Czech Republic

[7]The Czech Academy of Sciences, J. Heyrovsky Institute of Physical Chemistry, Dolejskova 3, 182 23 Prague 8, Czech Republic

1

[8]Department of Physics, Balikesir University, Balikesir 10145, Turkiye

[9]Department of Bioengineering, University of California, Los Angeles, Los Angeles, California 90095, United States

[10]Department of Materials Science and Engineering, University of California, Los Angeles, Los Angeles, California 90095, United States

Abstract

Isomers adsorbing with opposite orientations of their dipoles on surfaces are co-deposited to form mixed monolayers where both lateral dipole-dipole and lateral thiol-thiolate (S-H···S) interactions provide enhanced stability over single components. We demonstrate the ability to map individual isomers within mixed self-assembled monolayers of carboranedithiols on Au{111}. The addition of methyl groups to one isomer provides both an enhanced dipole moment and extra apparent height for differentiation via scanning tunneling microscopy (STM). Computational investigations provide rationalization of favorable interactions of mixed pairs and associated stability changes that arise from these interactions. Both STM images and Monte Carlo simulations yield similarly structured mixed monolayers, where approximately 10% of the surface having reversed dipole moment orientation leads to a homogenous monolayer with no apparent phase separation. By depositing the molecules under basic conditions, the lateral S-H···S interactions are suppressed while accentuating dipole-dipole forces. The investigated molecular system is composed of isomeric molecules with opposite orientations of dipoles and identical surface packing, which enables mapping individual molecules within the mixed monolayers and enables analyses of the contributions of weak lateral interactions to the overall stability of the assemblies.

2

Introduction

Self-assembled monolayers (SAMs) form ordered two-dimensional (2D) arrays *via* the adsorption of a headgroup onto a surface.[1,2] These SAMs provide frameworks for studying intermolecular forces in controlled environments.[3-6] The structures and properties of self-assembled materials are influenced by packing interactions similar to those observed in single crystals, where they are commonly referred to as packing forces.[7,8] Generally, it is these interactions that stand behind differences between the properties of a single molecule on one hand and an array of molecules in their bulk form on the other. Our previous work demonstrated that carboranethiols are a natural choice for investigating surface properties given their rigid, regular packing structures and tunable surface properties and applications to organic electronics.[9-13] Previous work investigated the roles of dipoles in self-assembly, but surprisingly, it is difficult to map different isomers within mixed monolayers as we aimed to do in this study.[14-17]

In complex structures, it is natural to analyze strong interactions first and understand their role in the self-assembly, be it either the supramolecular framework of molecules in a single crystal or the geometrical surface pattern of a 2D array of molecules immobilized on a surface. In the latter system, anchoring thiol groups strongly interact with the surface and limit the molecules by orienting them in a specific way, thus exposing them to a variety of lateral interactions.[10] van der Waals interactions are relatively strong lateral forces, which reflect molecular geometry and space requirements, leading to specific surface patterns.[18-20] Any material's structure and function is thus pre-determined by competing forces that play active roles during adsorption or, more generally, during the self-assembly process. Understanding these interactions is essential for designing new materials of desired structure and properties. Other groups have studied the interplay between hydrogen bonding and van der Waals interactions in aromatic monolayers, but here, we investigate a different pair: dipole-dipole forces and lateral hydrogen interactions of thiol/thiolate anchoring groups.[21,22]

Here, we use an adjusted carboranedithiol-based system, originally introduced and developed for SAMs in our laboratories,[10,23] to look further into 2D self-organized structures by changing only the properties we wish to investigate through cage dipole orientation and magnitude while keeping the SAM geometry and bonding scheme identical. In comparison, the common system of organic thiols is insufficient for these purposes as changes of

3

dipole moments in organic molecules are usually associated with significant changes of the molecular structure and/or changes of steric requirements.[14,24,25] We build on a significant advantage of the carborane molecular system to substitute certain fractions of molecules in the respective SAMs with those of different electron density distributions, without changing the surface geometrical pattern.[11,13] Such systems have the potential to reveal the effects of different dipole orientations and magnitudes of the molecules on their close neighbors and beyond and to unveil the existence of dipole-driven patterns within geometrical molecular arrangements.

Results and Discussion

The step necessary in these efforts was to develop the means to differentiate and to identify individual isomers within mixed SAMs so as to enable molecular mapping. We previously investigated the binding modes of 9,12-$(SH)_2$-1,2-$C_2B_{10}H_8$ (**O9,12**) and 1,2-$(SH)_2$-1,2-$C_2B_{10}H_8$ (**O1,2**) *via* scanning tunneling microscopy (STM), scanning probe spectroscopic imaging, and lower resolution surface-sensitive techniques. These molecules provide a template to investigate the roles of dipoles and lateral interactions in SAMs, as they have oppositely oriented dipoles but identical packing with nearest-neighbor spacings of 7.6 Å.[10] The two isomers are practically indistinguishable under ambient conditions when co-deposited in a SAM, so to solve this problem we have labelled **O9,12** molecules with two methyl substituents at the carbon atoms of the carborane backbone. All three molecules, with their abbreviations as well their complete chemical formulas, are depicted in **Figure 1**. Once assembled on gold surfaces, this dimethyl derivatization changes only the longitudinal space requirement of the parental **O9,12** molecule, *i.e.*, potentially increases the apparent height of these molecules in STM images, while maintaining lateral spacing requirements without disrupting the lateral molecular packing.

Structural and electronic properties of diMe-O9,12 (1,2-$(Me)_2$-9,12-$(HS)_2$-1,2-$C_2B_{10}H_8$)

Several methods, including computational and X-ray structural analyses, were used to investigate the structure of the new, dimethyl-labelled derivative, **diMe-O9,12**, and its differences compared to the parental **O9,12** (= 9,12-$(HS)_2$-1,2-$C_2B_{10}H_{10}$). *Ortho*-carborane, **O9,12,** and the dimethylated derivative of **O9,12**, *i.e.*, **diMe-O9,12**, have a two-fold symmetry axis. The thiol groups of **O9,12** form a bridging intramolecular hydrogen bond -S-

4

H···*S*(H)- shown in **Figure 2** that is absent in **O1,2**. Attaching thiol (–SH) and methyl (–CH₃) groups to the *ortho*-carborane skeleton leads to generally longer interatomic distances between the skeletal atoms. While these changes have an experimentally proven effect on decreasing the thermal rearrangement temperature of the carborane skeleton from *ortho*- to *meta*- to *para*- isomers,[26] they are too subtle to have significant effects on the geometries of the 2D monomolecular assemblies of these molecules on flat Au{111} surfaces, where they retain the nearest neighbor distances of approximately 7.6 Å.[10] Selected structural parameters, obtained experimentally from the single-crystal X-ray diffraction and also computationally (both available in the Supplementary Information), of **diMe-O9,12** are presented in **Table 1** and sketched in **Figure 2**. In addition, a side-view and a top-view of the space-filling computationally optimized model of the molecule are shown. The top view is compared to a circle representing the experimental surface area occupied by one molecule on the surface. The orientation of both methyl groups is longitudinal, protruding above the rigid cages in monolayers, and thus serves as a suitable label of **O9,12** molecules in mixed SAMs with the **O1,2** isomer. We note that both methyl groups, attached to the adjacent carbon atoms, are so close to one another that they can potentially rotate only as cog-wheels.[27] The positive inductive effect of the methyl groups further increases the dipole moment from ~5.5 D of the parental **O9,12** to 7.12 D, which makes this derivative exhibit potentially stronger lateral dipole-dipole interactions compared to its non-labelled analogue.[28]
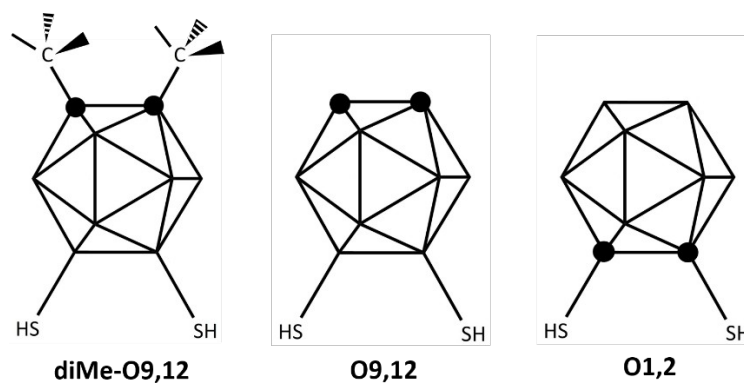

Figure 1. Schematic representation of carboranedithiols: **diMe-O9,12** = 9,12-(HS)$_2$-1,2-(CH$_3$)$_2$-1,2-C$_2$B$_{10}$H$_8$, **O9,12** = 9,12-(HS)$_2$-1,2-C$_2$B$_{10}$H$_{10}$, **O1,2** = 1,2-(HS)$_2$-1,2-C$_2$B$_{10}$H$_{10}$. Hydrogen atoms at the vertices of the clusters are omitted for clarity.

Table 1. Selected intramolecular distances in Å (See **Figure 2**) in **diMe-O9,12**, **O9,12**, and isomeric **O1,2** for comparison.

Intramolecular distance	O1,2	O9,12	diMe-O9,12
S-S	3.459	3.778, 3.823[a]	3.810, 3.777[b]
C(1)-C(2)	1.693	1.629, 1.640[a]	1.647, 1.675[b]
B(9)-B(12)	1.781	1.796, 1.797[a]	1.792, 1.781[b]
C(Me)-C(Me)	-	-	3.097, 3.141[b]
B(4)-B(7)	3.395	3.387, 3.380[a]	3.359, 3.340[b]

[a]Previously published single-crystal data;[29] [b]single-crystal data, the cif file can be found in the Supporting Information.
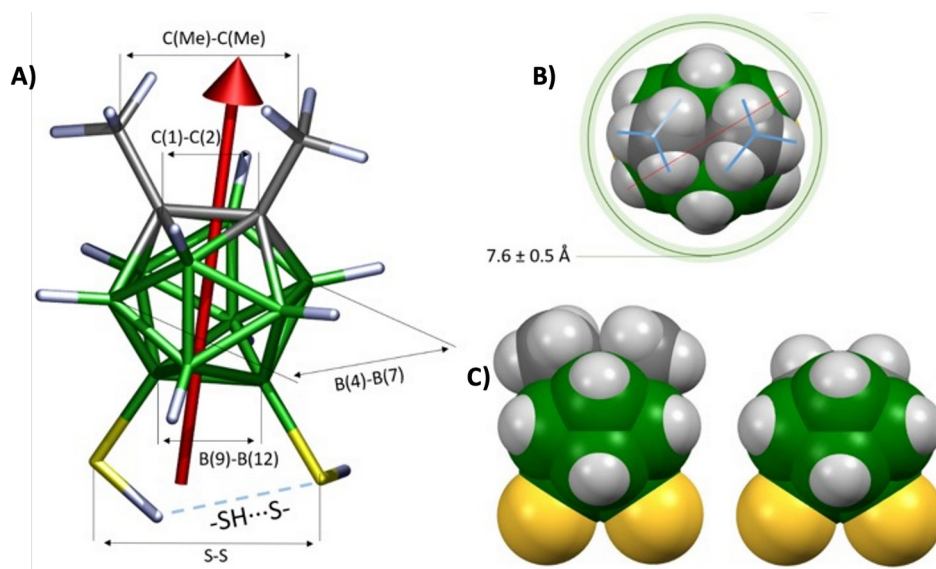

Figure 2. **A)** Computationally optimized structure with selected intramolecular distances, a schematic projection (red arrow) of the dipole moment (7.12 D), and the intramolecular -SH···S(H)- hydrogen bond sketched. **B)** Top view of a space-filling model with the scanning tunneling microscopy-determined nearest neighbor distance of 7.6 ± 0.5 Å for **O9,12** presented as a green circle. **C)** Side view comparison of **diMe-O9,12** with the respective parental **O9,12** space-filling models.

Supramolecular structures

Supramolecular structures of thiolated carboranes are usually dominated by hydrogen bonds between the respective thiol groups and CH vertices of the carborane cage(s).[26,29,30] In the case of **diMe-O9,12**, in which the relatively acidic hydrogen atoms at the CH vertices are replaced with methyl groups, it is the relatively strong dipole moment of the molecule together with its molecular geometry that leads to a specific single-crystal supramolecular arrangement. This structure consists of separated layers of molecules without any short contacts or hydrogen bonds connecting the layers. Interestingly, all molecules within one layer are arranged with their two-fold symmetry axes perpendicular to the plane of the layer and in rows with alternating dipole moments. **Figure 3** shows the "layered" supramolecular structure with the alternating orientation of molecules and so with their alternating dipole moments within the layer too. Monte Carlo optimized orientation of molecules within a monolayer shows dipole moments oriented perpendicularly to the plane and either up or down, in agreement with the experimentally determined single-crystal arrangement. The molecules with alternating dipole orientations, as observed in a single crystal, are arranged in infinite parallel lines while in the Monte Carlo simulated arrangement the lines of molecules oriented either up or down exhibit random changes in their propagation across the plane.
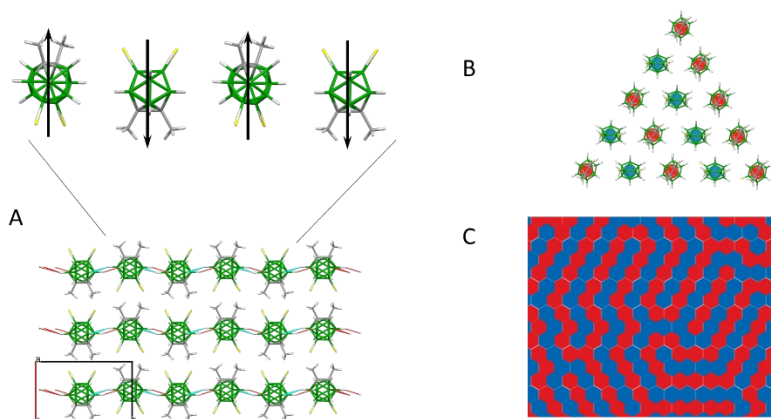

Figure 3. Layered supramolecular arrangement of molecules in a single crystal. **A)** Three layers only with short contacts within each layer depicted (bottom), and four molecules showing an alternating dipole-dipole driven arrangement within one layer. **B)** Top view of a fraction of 15 molecules from one layer with either red or blue background to demonstrate the alternating

dipole moment orientation. **C)** Computationally optimized arrangement of dipoles in a 2D layer with only two possible orientations, up or down shown as red or blue.

Scanning Tunneling Microscopy of Pristine diMe-O9,12 SAM on Au{111}

Monolayers of **diMe-O9,12** molecules were assembled on Au{111}/mica substrates under two different experimental conditions: neutral, from an EtOH solution; and basic, from an EtOH solution with equimolar amount of sodium hydroxide to deprotonate both SH groups prior to their surface adsorption. Both deposition conditions lead to an array of molecules with identical hexagonal surface arrangements and nearest neighbor distances of 7.6 ± 0.5 Å. Under neutral conditions, which we report first, STM imaging revealed *ca*. 10% of molecules protruding from the monolayer surface (**Figure 4A,B**). Previous measurements of its parent **O9,12** SAM showed almost no protruding molecules, ~98 ± 1 % of molecules were identified as monovalent (with only one thiol group deprotonated) on the surface, and 2 ± 1 % of molecules being adsorbed as divalent (both sulfhydryl groups deprotonated as thiolates).[10] The greater dipole moment of **diMe-O9,12** compared to **O9,12** manifests by even weaker acidity of the sulfhydryl groups, suggesting that the **diMe-O9,12** molecules might adsorb also as dithiols without deprotonation, as shown in **Figure 4D** (on the left). Deposition under basic conditions, serving in this case also as a comparative reference sample, led to a hexagonally packed SAM with no protrusions, shown in **Figure 4C**, and optimized geometry presented in **Figure 4H**.
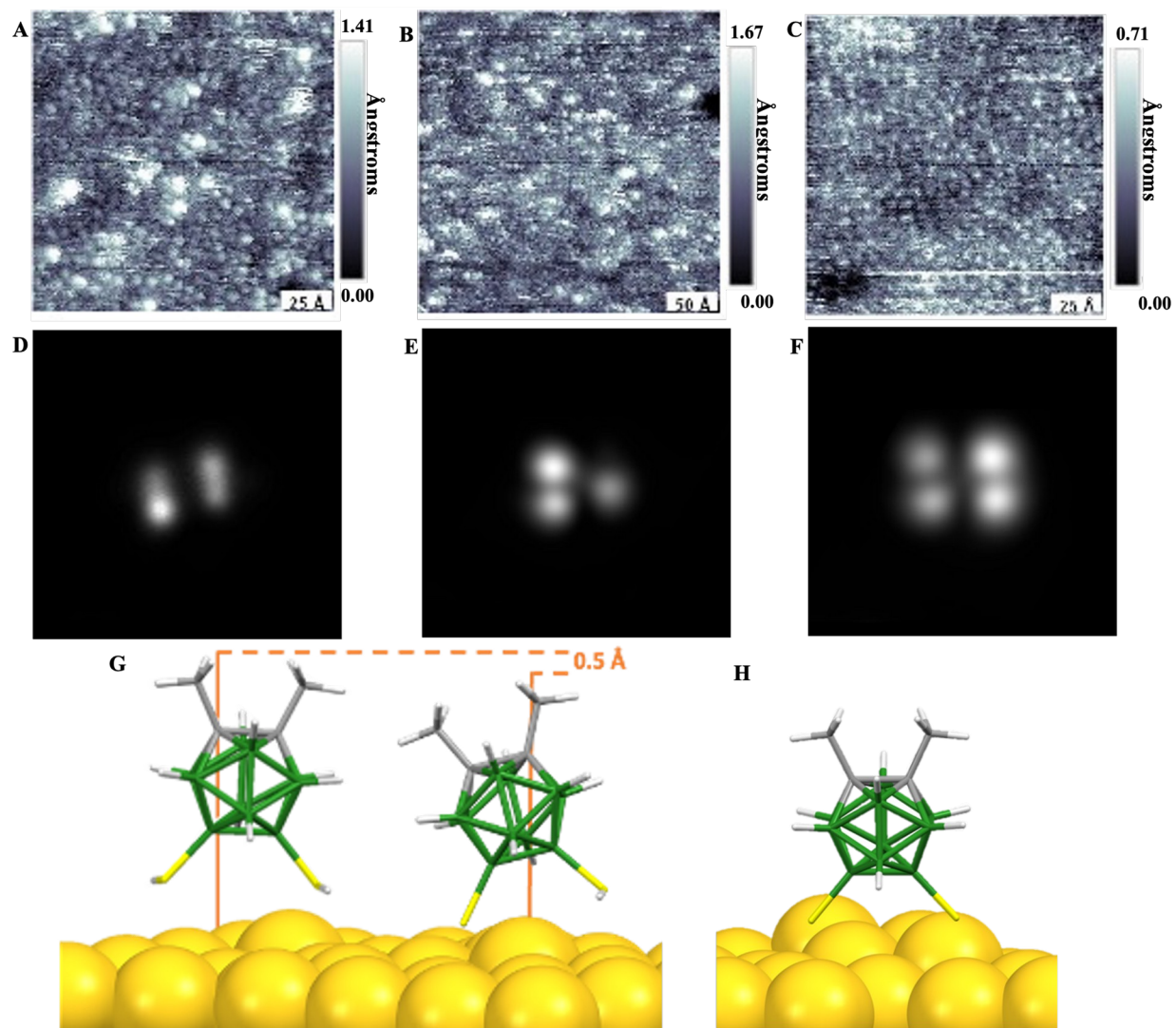
Figure 4. **A-C)** Scanning tunneling microscope (STM) images of pristine **diMe-O9,12** self-assembled monolayer deposited **A,B)** under neutral (V_{sample} = -0.1 V, $I_{tunneling}$ = 75 pA, T = 298 K) and **C)** basic (V_{sample} = -0.1 V, $I_{tunneling}$ = 100 pA, T = 298 K) deposition conditions on Au{111} at two different resolutions. **D-F)** Simulated STM images with the respective **D)** zerovalent, **E)** monovalent, and **F)** divalent binding modes. **G)** Schematic depiction of two distinct, computationally optimized binding modes indicating the apparent height difference of 0.5 Å observed under neutral deposition conditions. **H)** Computationally optimized geometry of the dithiolate binding mode achieved by depositing molecules under basic conditions.[10]

Previously, we reported on the differences in the apparent heights of adsorbed molecules of **O1,2** and **O9,12** in their SAMs, and we analyzed the inverted contrast in STM images for **O9,12** SAMs in which molecules bound as divalent appeared more protruding from the surface despite having their

9

geometrical height lower compared to the monovalent bound molecules. This particular aspect of adsorption is investigated further and verified in this study by demonstrating that molecules of **diMe-O9,12**, being weaker acids than **O9,12** (*i.e.*, showing even lower tendency to lose the sulfhydryl protons), adsorb predominantly as zerovalent (physisorbed dithiols) and appear less protruding in STM images of the respective SAMs, as confirmed by simulated STM images of all three binding modes of **diMe-O9,12** molecules presented in **Figure 4D-F**. The presence of both thiol- and thiolate-adsorbed moieties in the SAM was further proved by XPS with the respective binding energy values of S2p photoelectrons at 161.7 eV and 163.0 eV as shown in Table 2. The latter value is the same as in crystalline **O9,12** derivative.

Table 3. Measured core-level binding energies in eV and full width half maxima (parentheses) for Au films modified with **diMe-O9,12** and for a solid crystalline sample of **O9,12** for comparison.

Sample	**O9,12** (crystalline sample)	**diMe-O9,12** SAM/ Au
Stoichiometry	$B_{10}S_{2.1}C_{2.1}$	$B_{10}S_{2.2}C_{5.6}$
S $2p_{3/2}$	162.9 (2.2)	161.7 (1.1), 163.0 (1.1)
B 1s	189.7 (2.5)	189.6 (1.8)
C 1s	286.6 (2.3)	285.3 (1.5), 286.7 (1.6)

Lateral Molecular Interactions Analysis in Mixed SAMs

Lateral interactions in SAMs cover those of carboranes' backbones as well as interactions of their anchoring groups. To understand stabilizing or destabilizing effects, we have carried out calculations of isomeric pairs of molecules in vacuum and also adsorbed on gold surfaces.

Pristine and Mixed Pairs of Free Molecules

SH anchoring groups and their SH···S(H) intermolecular interactions

Understanding experimental results obtained with mixed monolayers of **O1,2** and **O9,12** (or its dimethyl-labelled analogue: **diMeO9,12**) requires

analyzing their lateral intermolecular interactions. To disentangle these interactions that take place in the respective 2D arrays, we first computationally investigated pairs of free molecules (both pristine and mixed) by copying their dipole moment orientations and nearest neighbor distances from an array on a gold surface but omitting their interactions with the gold surface in our first approximation, thus focusing purely on lateral interactions within the respective pairs. All three species and their respective SAMs have several common features: 1) similar, or practically identical, molecular geometry with a two-fold symmetry axis as shown and discussed above (**Figures 1** and **2**); 2) they all assemble into a hexagonal close-packed pattern on a gold surface (**Figure 4**) with identical nearest neighbor distances; 3) they all have relatively strong dipole moments, and by far the strongest in the case of **diMe-O9,12** molecule at 7.12 D; and 4) their sulfhydryl groups' acidities manifest strong electron-donating (**O9,12** and **diMe-O9,12**) and withdrawing (**O1,2**) effects, depending on to which vertices the SH groups are attached.

Two molecules positioned as close to each other as found on a gold surface, *ca*. 7.6 Å, can interact through their molecular backbones by their dipole-dipole moments and through structural elements such as their surface-anchoring thiol groups.[13] The latter can form intra- as well as intermolecular hydrogen bonds. To evaluate these lateral interactions and estimate their contributions to how homogeneously the molecules distribute in a SAM, we carried out calculations, the results of which are depicted in **Figure 5** (with all the results summarized and presented in **Table S3** and **Figure S9**). These results demonstrate significant differences in the strengths of mutual interactions in different molecular pairs.

The interactions between two carboranedithiol molecules are dominated by those between their thiol groups, specifically between a thiol hydrogen of one molecule and a sulfur of another. This intermolecular interaction is stronger and more stabilizing in the case of two molecules of **O9,12** than in two molecules of **O1,2**. However, by far the strongest case is a mixed pair with the interaction between the hydrogen of a thiol group bound to a skeletal carbon atom (C-S-H) of **O1,2** and the sulfur bound to a boron atom (B-S) in **O9,12**. The opposite orientation of the -SH···S- hydrogen interaction, *i.e.*, from the hydrogen of a boron-bound thiol group (B-S-H) of **O9,12** to a carbon-bound sulfur (C-S) of **O1,2**, is significantly weaker, as shown in **Figure 5e**. Correspondingly, the optimized structure of a single free molecule of **O9,12** shows an advantageous intramolecular -S*H*···*S*(H)-hydrogen bond between its thiol groups (**Figure 2**) while the molecule of

O1,2 does not. These computational results are consistent with the electron-donating effects of the carborane moiety at its skeletal boron positions and electron-accepting effects at the skeletal carbons while simultaneously elucidating these electronic effects' contributions to maximize the distributions of molecules in mixed self-assembled monolayers.

Fittingly with the advantageous orientation of two dipoles, parallel but oppositely oriented dipole moments in a mixed pair of molecules (**O1,2** and **O9,12**) are significantly more stable compared to their pristine pairs in which dipole moments are also parallel but oriented in the same direction.[31] Moreover, in the pair of **O9,12** molecules calculated in a conformation unsuitable for (*i.e.*, without) intermolecular hydrogen bonding (**Figure 4c**) to eliminate its stabilizing effects, the interactions between the two molecules were found to be repulsive, which we attribute to destabilizing parallel interactions of their relatively strong dipole moments.

In the mixed pairs, these results demonstrate a synergic effect of two types of lateral interactions: the molecules' anchoring SH groups as one and the molecular backbones *via* their dipole moments as the other, both leading towards greater stability of mixed pairs.
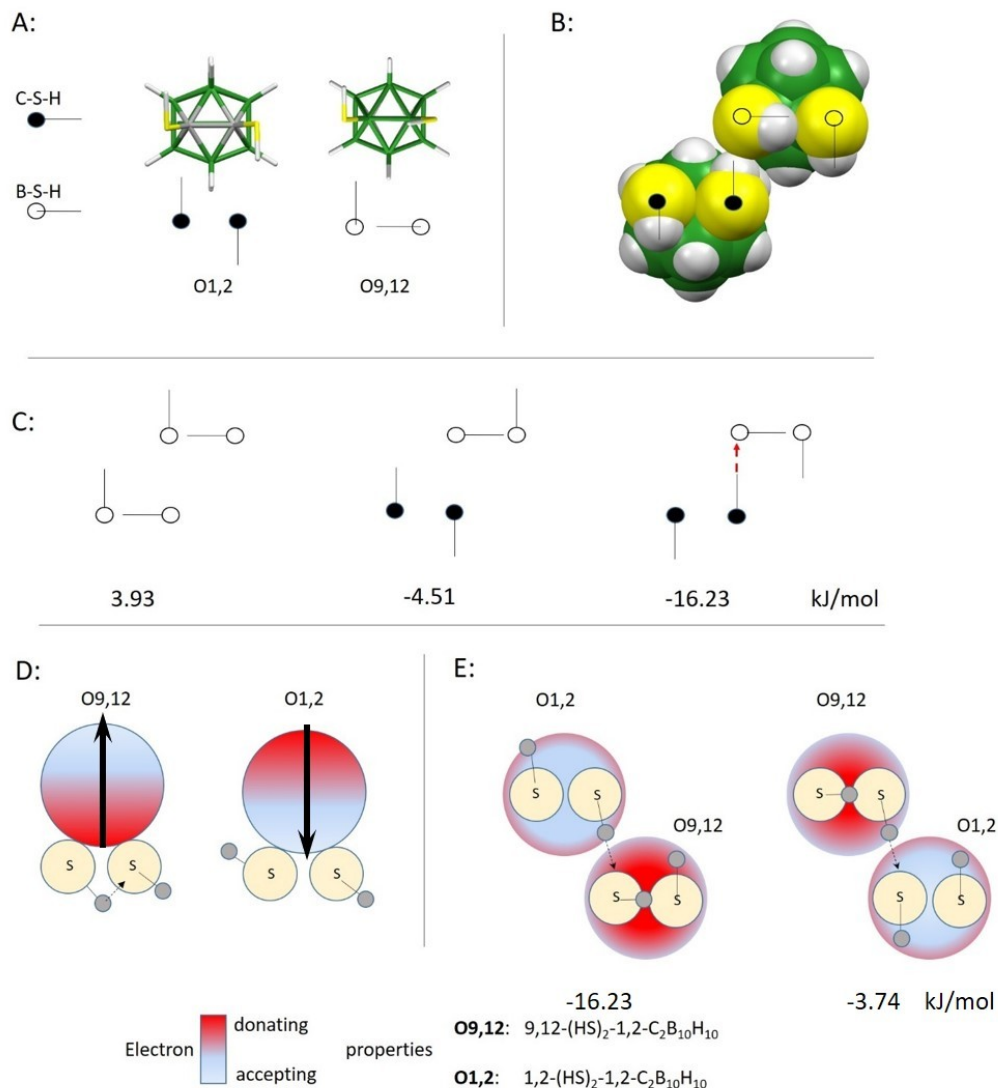
Figure 5. **A)** Computationally optimized isomeric carboranedithiols of **O1,2** and **O9,12** with sulfhydryl group conformations in their global energy minima. **B)** Space-filling model of a pair of molecules of **O1,2** and **O9,12** exhibiting intermolecular C-*SH*···*S*(H)B interaction. **C)** Schematic representation of three mixed pairs of **O1,2** and **O9,12** showing for simplicity only the sulfhydryl groups and their particular conformations. The pairs on the left and in the middle are calculated with no intermolecular *SH*···*S* interactions while the one on the right does include this interaction. The full black dots represent sulfur atoms attached to the carbon vertices of the carborane clusters, the hollow dots represent sulfur atoms attached to the boron vertices of the carborane clusters. **D)** Side view schematic of both isomers showing electron-donating (red) and accepting (light blue) properties

of the carborane scaffold with the respective dipole moment orientation. **E)** Bottom view of two mixed pairs with -*SH···S*- interactions.

Pristine and Mixed Pairs of Molecules on Au(111)

The previously discussed analyses of intermolecular interactions in free pairs of molecules, oriented in a similar fashion as on a gold surface, do not, as a first approximation, cover the interactions with gold surfaces. Therefore, a set of calculations with several pairs of molecules adsorbed on 7×4 gold slabs was carried out to investigate the surface adsorption effect. Considering the adsorption energies summarized in **Table 2**, a pair of **O9,12** molecules show the greatest stability (adsorption energy of -9.11 eV), followed by the two pairs of mixed molecules of **O1,2** and **O9,12**, and the least stable pair is represented by two molecules of **O1,2** on a gold surface. This particular order results from the stabilizing effects of B-S-Au bonds, which are significantly more stable than the respective C-S-Au bonds. The ratio of B-S-Au to C-S-Au bonds in the investigated pairs follows the trend observed in the adsorption energies: 3:0 in a pair of two **O9,12** molecules (**Figure 6B**); 2:1 in a mixed pair of **O1,2** and **O9,12** (**Figure 6C**); 1:2 in a pair of **O9,12** and **O1,2** (**Figure 6D**); and 0:3 in a pair of two **O1,2** molecules (**Figure 6A**). However, the adsorption energy value does not show the stabilizing or destabilizing effects of lateral interactions, which are more important for understanding the 2D patterns of SAMs. To assess the lateral forces between two molecules in the respective pairs, we calculated the pair interaction energies using the following equation: $E_{\text{pair interaction on Au/111}} = E_{\text{pair on Au/111}} - E_{\text{dithiol 1 on Au/111}} - E_{\text{dithiol 2 on Au/111}} + E_{\text{Au/111 slab}}$, and sorted the pairs accordingly. These results cover both the lateral hydrogen-bonding interactions of anchoring groups influenced differently by carborane backbones *via* their electron-withdrawing and -accepting properties as well as direct dipole-dipole interactions of the molecular backbones. The mixed pairs of molecules **O1,2** and **O9,12** (**Figure 6C**) show the greatest stabilizing effects with the pair interaction energy of -0.22 eV, followed by the second mixed pair of molecules **O9,12** and **O1,2**, then the pair of molecules of **O1,2**, and the least stable, a pair of two molecules of **O9,12**, which represent two molecules with strong dipole moments aligned disadvantageously in the same direction. These results follow the trend discussed above for the computational investigation of free pairs of molecules.

As discussed above and further observed with more experimental STM results, Figure S7 in the Supporting information, the mixed SAMs of **O1,2** and **O9,12** (or the **diMe-O9,12**) deposited under neutral conditions lead to

14

images where it is difficult to assign the individual molecules due to their distinct binding modes. Therefore, in another experiment, we focused on mixed SAMs of **O1,2** and **diMe-O9,12** as two molecules providing the greatest possible apparent height difference in STM images after deposition under basic conditions to maximize the fractions of molecules that adsorb in the divalent mode only. In addition, the basic deposition avoids any possibility for interactions between the anchoring groups *via* their hydrogen - S*H*···*S*(H)- bonds due to prior deprotonation of the SH groups. As a result of both labelling **O9,12** molecules with two methyl groups as well as the basic deposition conditions, we assign the more protruding molecules in the experimental STM images, **Figure 8**, to the molecules of **diMe-O9,12** distributed in the monolayer with no phase separation due to dipole-dipole interactions. The homogeneous distributions of **diMe-O9,12** molecules in the matrix of **O1,2** in the SAM has been further addressed and supported by Monte Carlo simulations, which show, in good agreement with experiment, the ideal separation of molecules with dipoles being oriented opposite to the orientation of the remaining matrix.
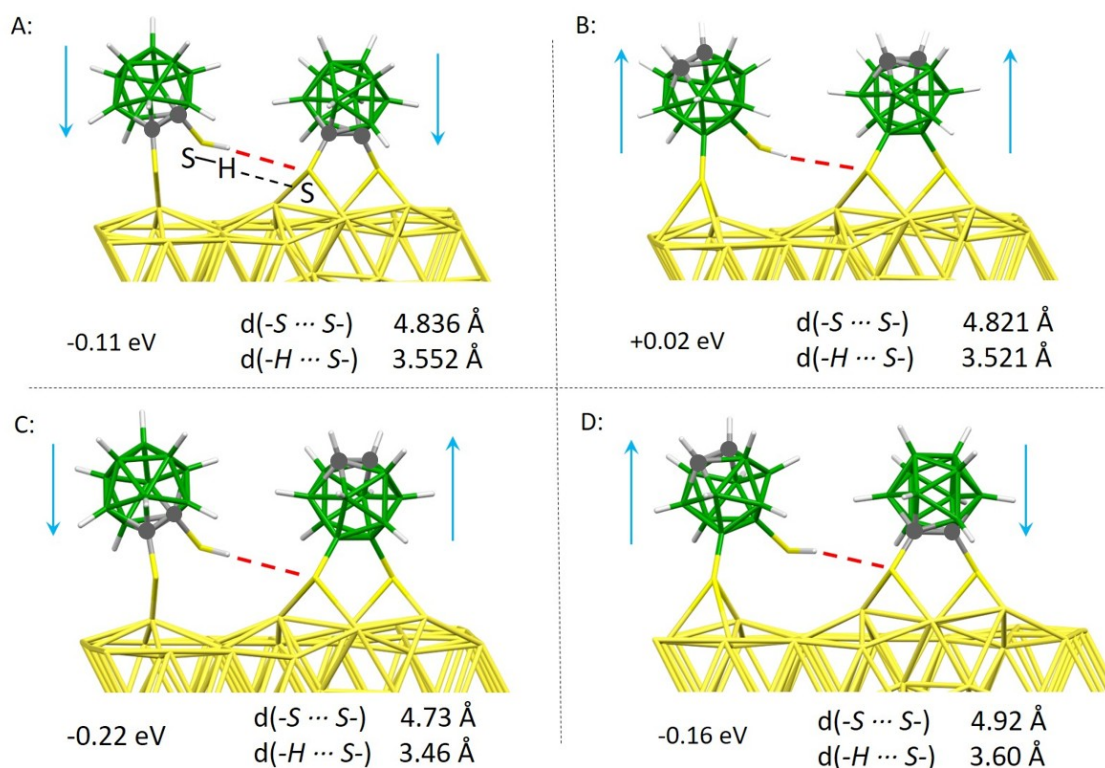

Figure 6. Computationally optimized pairs of isomeric carboranedithiols, **O1,2** and **O9,12**, on a gold surface with -S-H···S- hydrogen interactions indicated. **A)** An **O1,2** and **O1,2** pair, **B)** an **O9,12** and **O9,12** pair, **C)** an

15

O1,2 and **O9,12** mixed pair, and **D)** an **O9,12** and **O1,2** mixed pair. The lateral pair interaction energy is shown in eV. Larger grey dots indicate the positions of carbon atoms in the carborane cage backbones.

Table 3. Calculated adsorption and interaction energies in eV of pairs of molecules on Au{111} (7 × 4). More detail is provided in the Supporting Information.

Pair: dithiol1-dithiol2	**O1,2-O1,2**	**O9,12-O9,12**	**O1,2-O9,12**	**O9,12-O1,2**
E $_{pair\ adsorption\ on\ Au\{111\}}$	-8.86	-9.11	-8.95	-8.87
E $_{pair\ interaction\ on\ Au\{111\}}$	-0.11	0.02	-0.22	-0.16

Surface Potential Changes

We used scanning Kelvin probe force microscopy (SKPFM) to investigate surface potential changes as a measure of dipole moment magnitude and orientation of the molecules on the surface.[31] **Figure 7** shows a comparison of the new derivative, **diMe-O9,12**, compared to a bare metal surface and to surfaces modified with **O1,2** and **O9,12**. In agreement with the orientation and magnitudes of the dipoles, the **O1,2** SAM significantly decreases the surface potential of the metal substrate, while **O9,12** increases the value, and **diMe-O9,12** increases it even more. The surface potential shift shows the effect of the orientation and the relative dipole strength of **diMe-O9,12** and the respective SAM.
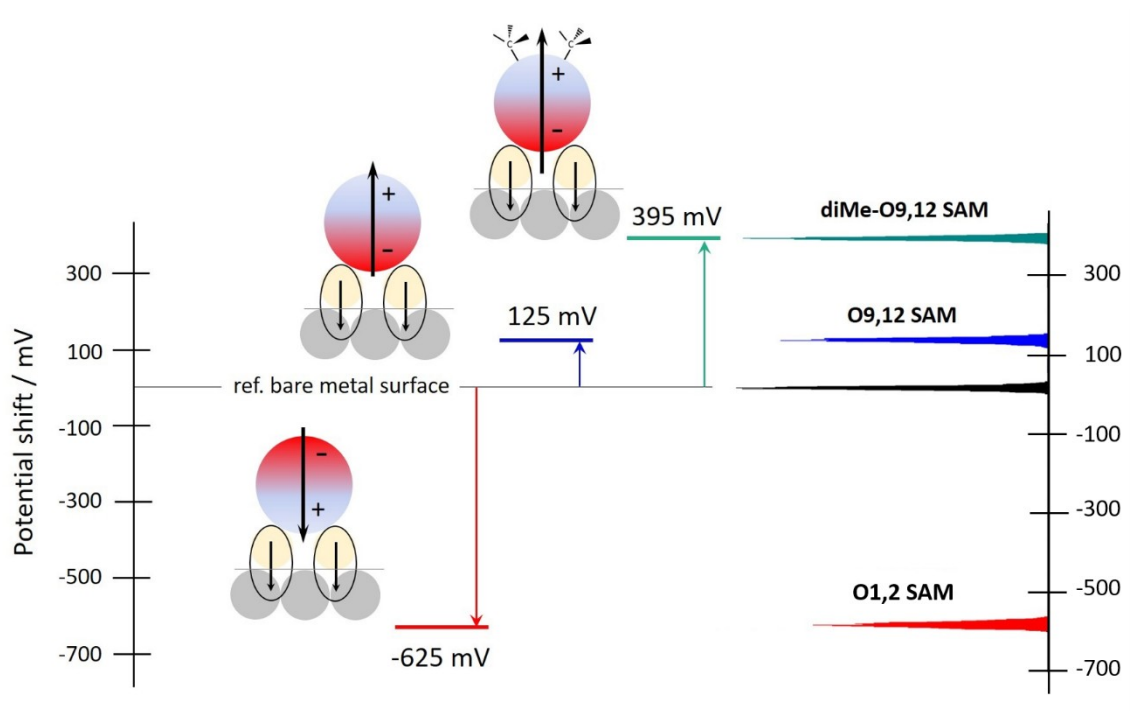
Figure 7. Surface potential shifts caused by SAMs of **O1,2**, **O9,12**, and **diMe-O9,12** with the respective histograms (on the right) showing narrow distributions of values as analyzed using scanning Kelvin probe force microscopy.
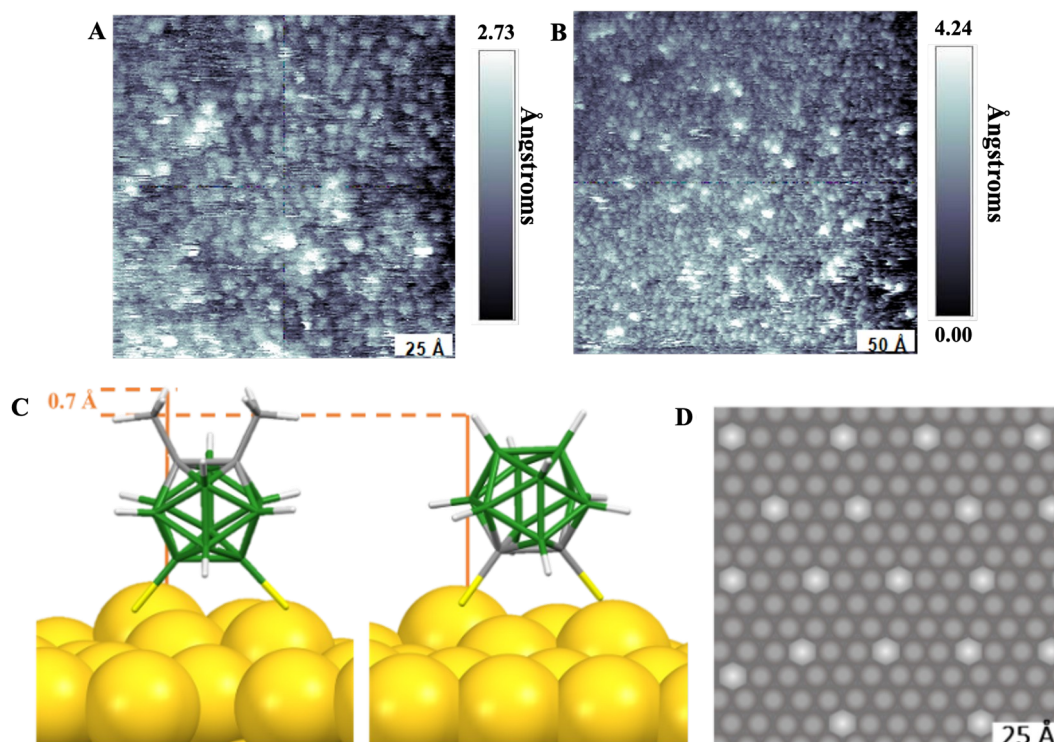
Figure 8. **A,B)** Scanning tunneling microscope (STM) images of a mixed **diMe-O9,12** and **O1,2** (9:1) SAM deposited under basic conditions on Au{111}/mica at two different resolutions ($V_{sample} = -0.1$ V, $I_{tunneling} = 105$ pA, T = 298 K. **C)** Schematic of two distinct binding modes with an apparent height difference of 0.7 Å in STM images. **D)** Result of dipole-dipole interactions simulation in a hexagonal field with 10% of molecules having the opposite dipole moment orientation.

Conclusions and Prospects

We have designed and characterized a new derivative of 1,2-dicarba-*closo*-dodecaborane-9,12-dithiol (**O9,12**), which was used previously as a constituent of self-assembled monolayers demonstrating how the SH group acidity influences its scheme of adsorption. The new derivative, 1,2-dimethyl-1,2-dicarba-*closo*-dodecaborane-9,12-dithiol (**diMe-O9,12**), which is a version of its parent molecule labelled with two additional methyl groups, has exhibit identical lateral steric requirements in its respective SAMs as the parent derivative, and as its isomeric 1,2-dicarba-*closo*-dodecaborane-1,2-dithiol (**O1,2**). The two methyl groups increase the longitudinal steric demands of the **O9,12** molecule making it more easily distinguishable from its **O1,2** isomer in STM images. The new derivative has been structurally characterized using single-crystal diffraction analysis, which revealed a

supramolecular structure driven by dipole-dipole interactions, fittingly with the large dipole moment of the molecule (7.12 D). When deposited on a gold surface under neutral conditions, the pristine SAMs of this derivative show that the molecules adsorb 90% in zerovalent mode (*i.e.*, as fully physisorbed dithiols) and 10% in monovalent mode. The molecules adsorbed in the less abundant monovalent mode appear more protruding in STM images, as confirmed by simulations. When deposited under basic conditions, all molecules of the pristine **diMe-O9,12** SAM were adsorbed as divalent (*i.e.*, as fully chemisorbed dithiolate moieties) without any significantly differing apparent heights. In this study, within the focus on lateral interactions within SAMs, we have analyzed two essential contributions: first, hydrogen-bonding interactions between the anchoring SH groups of adjacent molecules, and second, lateral dipole-dipole interactions driven mainly by the carborane backbones. Both interactions increase the stability of mixed SAMs consisting of two components of opposite dipole moment orientation, and lead to arrays of molecule with alternating dipoles. Experimental co-deposition of **O1,2** and **O9,12** (or **diMe-O9,12**) molecules under neutral conditions leads to monolayers with apparent protrusions affected by different binding modes of the individual constituents, which makes it difficult to assign the molecules to each isomer. Narrowing the problem by depositing molecules under basic conditions, thus avoiding the sulfhydryl group interactions, and by co-depositing **O1,2** with the labelled **diMe-O9,12** to increase their apparent height differences, enables identification of each molecule within the STM images of the SAMs. Consistent with dipole-dipole interactions in Monte Carlo simulations, the molecules are well separated and homogenously distributed over the surface within the mixed SAM. With this contribution, we have addressed a relatively complicated issue of disentangling weak interactions within SAMs, including the importance of dipole-dipole interactions that occur within many molecular self-assembled systems but largely unnoticed or hidden behind much stronger interactions.

Experimental

General Procedures, Chemicals, and Materials

General Procedures and Chemicals. Carboranedithiol derivatives (**O1,2** and **O9,12**) as well as 9,12-bis(methoxy-methylthio)-*o*-carborane starting precursor (herein further referred to as CB-MOM) for the synthesis of **diMe-O9,12**, were prepared according to the literature.[32] The purity was checked by gas chromatography with mass spectrometric detection (GC-MS) and by

^{11}B and ^{1}H NMR spectroscopy. Nuclear magnetic resonance spectroscopy was performed at room temperature on a Varian MercuryPlus at 400 MHz using standard techniques and procedures. Solvents for synthesis (such as THF) were purchased from Penta a.s. Czech Republic, and additionally dried with sodium in the presence of benzophenone (99.8%, purchased from Sigma-Aldrich) and freshly distilled before experiments. Other solvents were used as received. Solvents for STM experiments were purchased from Sigma-Aldrich and used as received. The NMR spectra were measured in CDCl3 (99.8% D) as received from Eurisotop.

Synthesis of diMe-O9,12

1,2-dimethyl-9,12-SMOM-o-carborane:

0.838 g (2.89 mmol) of CB-MOM were dissolved in 30mL of dry and freshly distilled THF under nitrogen atmosphere and cooled to 0 °C in ice-water bath. 2.34 mL (5.85mmol) of n-BuLi (2.5 M solution in hexanes) were added dropwise via a syringe. After 5 minutes, 0.825 g (5.81 mmol) of methyl iodide were added dropwise, still cooling, and stirred overnight at room temperature. The solvent was removed, the residue dissolved in diethyl ether and extracted twice with distilled water (30 mL). The solution was dried over anhydrous sodium sulfate and filtered through a layer of silica gel. Removal of the solvent by evaporation on a rotary evaporator gave viscous oil which slowly solidified. Yield: 1.205 g

1,2-dimethyl-9,12-(SH)2-o-carborane, **diMe-O9,12**

0.74 g (2.28mmol) of 1,2-dimethyl-9,12-SMOM-o-carborane were dissolved in 25 mL of acetonitrile/water (4:1). A solution of 1.251 g (4.61 mmol) mercury(II) chloride in 2-3 mL of acetonitrile/water (4:1) was added and the mixture was stirred for 2 hours. White
precipitate was collected by filtration and washed with 10 mL acetonitrile/water (4:1) and 10 mL of water. The solid product was suspended in chloroform and H_2S was bubbled through the suspension while a black precipitate is formed (HgS). The mixture was filtered using a syringe filter. Evaporation of the solvent gave white crude product which was further purified by sublimation under reduced pressure ($\sim 10^{-2}$ mbar) at 120 °C with the yield of 90%.

Experimental Methods

Scanning Tunneling Microscopy (STM)

Samples for imaging were prepared on Au{111}/mica substrates (Agilent Technologies, Santa Clara, CA), which were hydrogen-flame annealed with 10 passes at a rate of 0.4 Hz prior to monolayer deposition. Ethanol and NaOH pellets were used as received (Sigma-Aldrich, St. Louis, MO). Substrates were placed into a capped vial with 1 mL of a 1 mM solution of the respective isomer or mixture of isomers in ethanol for 24 h for deposition in neutral conditions. Samples deposited under basic conditions were only deposited for 10 min in order to decrease the possibility of degradation. After deposition, samples were cleaned with neat ethanol and dried with a stream of nitrogen gas three times before loading into the STM.

All STM measurements were performed with a custom-built Besocke-style with a platinum/iridium tip (80:20) in constant current mode under ambient conditions.[33]Samples were held at a fixed bias (V_{sample} = -0.1 V). The known lattice of the 1-dodecanethiolate SAMs on Au{111} was used for calibration. The STM image analysis was done using MATLAB (Mathworks, Natick, MA) and Gwyddion (http://gwyddion.net/).

Scanning Kelvin Probe Force Microscopy (SKPFM)

The samples were measured using a Bruker Icon ambient AFM with the standard amplitude-modulated Kelvin probe force microscopy (AM-KPFM) 2-pass method.[34,35] The first pass measured the topographic profile using tapping mode, then the AFM-probe was lifted up to 20 nm above the surface, and the second pass copied the profile saved during the first pass with the local contact potential difference (CPD) measured. Since the measured CPD is strongly affected by the probe tip shape and quality, the measurement workflow was set to maximally reduce the probe wearing effect. The number of scanned lines for each sample was limited to 10-20 lines (256 data points per line) and the final CPD value was taken from the distribution histogram. The reference sample was repeatedly measured, typically after each SAM sample, to control the quality of the tip. Each sample CPD measurement thus has the closest silver reference CPD measurement. The value of the potential shift caused by the SAM was calculated as the difference between the measured CPDs of a sample and the silver reference. For this purpose, the silicon BudgetSensors Multi75 cantilever with a force constant of ~3 N/m, and a resonant frequency of ~75 kHz was used. The radius of a new tip was expected about ~8 nm. The setpoint for the tapping mode was set as low as possible while enabling the feedback to follow the surface profile. The scanning speed ranged from 200 to 500 nm/s. All AFM measurements were

performed at ambient conditions, at about 25 °C and approx. 30% air humidity.

X-Ray Photoelectron Spectroscopy (XPS)

The X-ray photoelectron spectra (XPS) of the sample were measured using a modified ESCA 3 MkII multitechnique spectrometer equipped with a hemispherical electron analyzer operated in a fixed transmission mode. Al K_{α} radiation was used for electron excitation. The binding energy scale was calibrated using the Au $4f_{7/2}$ (84.0 eV) and Cu $2p_{3/2}$ (932.6 eV) photoemission lines. The pressure in the XPS analysis chamber during spectra acquisition was 6×10^{-9} mbar. The powdered sample was spread on an aluminum surface. The spectra were collected at a takeoff angle of 45° with respect to the macroscopic surface normal. Survey scan spectra and high-resolution spectra of B1s, C1s and S2p photoelectrons were measured. The spectra were curve fitted after subtraction of Shirley background using the Gaussian−Lorentzian line shape and nonlinear least-squares algorithms (CasaXPS software). Binding energies of the powdered sample were referenced to C 1s peak of adventitious carbon at 284.8 eV. Quantification of the elemental concentrations was accomplished by correcting the photoelectron peak intensities for their cross sections and for the analyzer transmission function. In calculations homogeneous composition of the analyzed sample layer was assumed. The typical error of quantitative analysis by XPS is ~10%.

Computational Investigations

Free pairs of molecules

Quantum chemistry calculations were performed by the NWChem[36] package. The geometries were optimized[37] by the means of the density functional theory with the hybrid exchange–correlation functional PBE0[38,39] using Jensen's double–zeta segmented polarization consistent basis set pcseg-1.[40]

Two molecules of *closo*-dicarbadodecaboranedithiol were placed in positions resembling their arrangement in a monolayer on a metal surface, the (approximate) planes formed by the sulfur atoms and C1, C2, B9, and B12 cage atoms of each molecule set parallel, and the four sulfur atoms situated in one plane perpendicular to those two in the pattern of the monolayer elementary cells. The sulfur atoms from the geometries as taken from our previous study were levelled.[10] The positions of the four sulfur atoms were then fixed, and the positions of all the other atoms optimized. Several

calculations were performed for each pair (1,2 + 1,2; 9,12 + 9,12; and 1,2 + 9,12) with different conformations of the thiol hydrogens to find the configuration with the minimum energy. Then, the energies of each of the molecules of such pairs were calculated separately in the geometry of the molecule in the optimized pair, with the atoms of the other molecule replaced by ghost atoms to preserve identical basis sets. The energy of interaction between the two molecules was calculated for each pair as the difference between the sum of the energies of the individual molecules, and the energy of the pair.

Pairs of molecules adsorbed on a gold surface

Theoretical studies, based on density functional theory (DFT), estimated quantifiable characteristics of carboranethiol SAMs on Au(111) consistent with experiments.[41] Following the same framework, dispersion corrected density functional theory (vdW-DFT) calculations were performed to gain further insight into the adsorption characteristics through atomistic modeling of isomeric carboranedithiols on the gold surface. The projector-augmented wave (PAW) method was used as implemented in VASP (version 6.3).[42–44] Variational minimization of the ground state energy of each model structure was achieved through plane wave basis expansion of the Kohn-Sham (KS) orbitals up to 400 eV cutoff. The exchange-correlation (XC) effects were taken into account by employing contemporary Strongly Constrained and Appropriately Normed (SCAN) functional which was proposed to heal numerical instabilities of the standard functionals of Generalized Gradient Approximation (GGA) by imposing additional constraints to reproduce accurate reference values.[45] Moreover, the intermolecular interactions within SAMs require consideration of the dispersive corrections. For this purpose, we incorporated revised Vydrov-van Voorhis (rVV10) non-local correlation energies as complemented in the modern SCAN+rVV10 functional.[46,47] This method not only gives a better estimation of the lattice constant of gold among standard and van der Waals (vdW) -supplemented DFT functionals, but also improves the description of metal-organic interface properties relative to benchmarked vdW-DFT functionals in comparison with the experiments.[47–50]

Periodic boundary conditions (PBC) were assumed and the (111) surface of gold was represented with four-layer slab models, which were built by replication of the bulk unit cell and then by termination through (111) planes to expose top and bottom faces. Matched and mixed pairs of **O1,2** and

23

O9,12 carborane-dithiols were considered on a (7 × 4) slab (with the dimension of 19.20 Å and 10.97 Å, respectively), and **diMe-O9,12** SAMs were modeled using a (4 × 4) slab (with two distinct binding modes as shown in Fig. 6D). Each computational supercell contains one of the slab models with one or more molecular adsorbates and a vacuum region with a height of at least 12 Å to avoid unphysical interaction between the periodic images of the slabs. We report the minimum energy geometries of molecules on the surface, which were determined by tracing all probable adsorption sites. The geometry optimizations were achieved by imposing a convergence criterion based on the minimization of the Hellmann-Feynman forces on each atom to be smaller than 10^{-2} eV/ Å. The Brillouin zone integrations were carried out over Γ-centered 6 × 6 × 1 and 3 × 6 × 1 k-point samplings for the (4 × 4) and (7 × 4) surface cells, respectively. Technically, occupations of the electronic states at the Fermi energy were smeared using the Methfessel-Paxton (MP) scheme with a parameter of 0.1 eV. The dipole corrections were also included in the polar slab calculations.

The lateral pair interactions between matched and mixed isomeric carboranedithiols of **O1,2** and **O9,12** on Au{111} (including -S-H⋯S- interactions, as shown in Fig. 4) were calculated using the (7 × 4) slab model with the expression:

$$E_{pair} \int ¿ = E_{AB/Au(111)} + E_{Au(111)} - E_{A/Au(111)} - E_{B/Au(111)} ¿ \; ,$$

where the first and the second molecules are labeled as A and B, respectively. $E_{AB/Au(111)}$ is the total supercell energy of the slab with the pair of adsorbates, $E_{Au(111)}$ is the energy of the clean slab. $E_{A/Au(111)}$, and $E_{B/Au(111)}$ are the energies of the gold slabs with the other adsorbate molecule of the pair is removed.

Computationally simulated STM images

The relaxation calculations were performed with projected augmented wave density functional theory (PAW-DFT) with the Vienna Ab-initio Simulation Package (VASP) version 5.4.4. The relaxation used a convergence parameter of 10^{-6} eV, Gaussian smearing with a sigma value of 0.1 eV, a plane-wave KE cutoff of 400 eV, and a 5 × 5 × 1 Monkhorst−Pack k-point grid. The geometry relaxation would continue until the forces on all atoms are below 0.01 eVÅ^{-1}.

Two Au(111) surfaces were modeled, with a 4 ×4 × 4 atom surface to study individual carboranes and a 4 ×7 ×4 atom surface to study two interacting carboranes, using a [10.97500,0,0]×[5.48750,9.50463,0]×[0,0,24.50000] Å supercell and a [19.20500,0,0]×[5.48750,9.50463,0]×[0,0,24.50000] Å supercell respectively, with four layers along z. The bottom two layers were fixed during the optimization for both cases. To be consistent with experiment, the calculated lattice constant for Au was chosen to be 2.95 Å. To prepare the STM images and the charge density plots, we continued using a 5 × 5 × 1 Monkhorst−Pack k-point grid. An energy range of -0.1 eV to E_F was used in the partial charge density calculations. Then, the STM images were simulated using the Tersoff-Hamann approximation and the program p4vasp, with a constant tip height of 19.3 Å.

Monte Carlo simulations

We performed simulated annealing simulations to explore the optimal distribution of dipoles with different orientations. Simulations were performed on 2D hexagonal lattices with lattice parameter a = 7.6 Å. 2D periodic boundary conditions were used. Dipole moments were set to 3.6 D and 5.7 D, respectively.

Ratio of dipoles with opposite orientation was fixed during the simulation and dipoles were randomly distributed in the lattice at the start of simulation. In each simulation step, we randomly chose two dipoles with opposite orientation and switched their positions in the lattice. We determined the energy difference ΔE connected with this switch. When the energy difference ΔE was negative, the new state was automatically accepted. In the case of positive ΔE, the probability of acceptance of this new state was

$$\exp\left(\frac{-\Delta E}{k_B T}\right),$$

where k_B is the Boltzmann constant and T is simulation temperature. The temperature progressively decreases from an initial value towards zero. Starting temperature is set to such a value that almost all new states are accepted. After a given number of simulation steps, the temperature is decreased and the simulation continues. At the end of the simulation the temperature limit is zero and only accepted changes lower the system energy. Because of long-range dipole interactions and the periodicity of simulation lattice, Ewald summation for confined geometries was used to determine the energy change.[51]

References

(1) Love, J. C.; Estroff, L. A.; Kriebel, J. K.; Nuzzo, R. G.; Whitesides, G. M. Self-Assembled Monolayers of Thiolates on Metals as a Form of Nanotechnology. *Chem. Rev.* **2005**, *105*, 1103–1170. https://doi.org/10.1021/cr0300789.

(2) Ulman, A. Formation and Structure of Self-Assembled Monolayers. *Chem. Rev.* **1996**, *96*, 1533–1554. https://doi.org/10.1021/cr9502357.

(3) Jiang, P.; Deng, K.; Fichou, D.; Xie, S.-S.; Nion, A.; Wang, C. STM Imaging *Ortho*- and *Para* -Fluorothiophenol Self-Assembled Monolayers on Au(111). *Langmuir* **2009**, *25*, 5012–5017. https://doi.org/10.1021/la803816u.

(4) Qi, Y.; Liu, X.; Hendriksen, B. L. M.; Navarro, V.; Park, J. Y.; Ratera, I.; Klopp, J. M.; Edder, C.; Himpsel, F. J.; Fréchet, J. M. J.; Haller, E. E.; Salmeron, M. Influence of Molecular Ordering on Electrical and Friction Properties of ω-(*Trans*-4-Stilbene)Alkylthiol Self-Assembled Monolayers on Au (111). *Langmuir* **2010**, *26*, 16522–16528. https://doi.org/10.1021/la100837g.

(5) Liao, L.; Li, Y.; Xu, J.; Geng, Y.; Zhang, J.; Xie, J.; Zeng, Q.; Wang, C. Competitive Influence of Hydrogen Bonding and van Der Waals Interactions on Self-Assembled Monolayers of Stilbene-Based Carboxylic Acid Derivatives. *J. Phys. Chem. C* **2014**, *118*, 28625–28630. https://doi.org/10.1021/jp509041b.

(6) Frey, S.; Stadler, V.; Heister, K.; Eck, W.; Zharnikov, M.; Grunze, M.; Zeysing, B.; Terfort, A. Structure of Thioaromatic Self-Assembled Monolayers on Gold and Silver. *Langmuir* **2001**, *17*, 2408–2415. https://doi.org/10.1021/la001540c.

(7) Yan, J.; Ouyang, R.; Jensen, P. S.; Ascic, E.; Tanner, D.; Mao, B.; Zhang, J.; Tang, C.; Hush, N. S.; Ulstrup, J.; Reimers, J. R. Controlling the Stereochemistry and Regularity of Butanethiol Self-Assembled Monolayers on Au(111). *J. Am. Chem. Soc.* **2014**, *136*, 17087–17094. https://doi.org/10.1021/ja508100c.

(8) Dameron, A. A.; Ciszek, J. W.; Tour, J. M.; Weiss, P. S. Effects of Hindered Internal Rotation on Packing and Conductance of Self-Assembled Monolayers. *J. Phys. Chem. B* **2004**, *108*, 16761–16767. https://doi.org/10.1021/jp049442d.

(9) Goronzy, D. P.; Staněk, J.; Avery, E.; Guo, H.; Bastl, Z.; Dušek, M.; Gallup, N. M.; Gün, S.; Kučeráková, M.; Levandowski, B. J.; Macháček, J.; Šícha, V.; Thomas, J. C.; Yavuz, A.; Houk, K. N.; Danışman, M. F.; Mete, E.; Alexandrova, A. N.; Baše, T.; Weiss, P. S. Influence of Terminal Carboxyl Groups on the Structure and Reactivity of Functionalized *m* -Carboranethiolate Self-Assembled Monolayers. *Chem. Mater.* **2020**, *32*, 6800–6809. https://doi.org/10.1021/acs.chemmater.0c02722.

(10) Thomas, J. C.; Goronzy, D. P.; Serino, A. C.; Auluck, H. S.; Irving, O. R.; Jimenez-Izal, E.; Deirmenjian, J. M.; Macháček, J.; Sautet, P.; Alexandrova, A. N.; Baše, T.; Weiss, P. S. Acid–Base Control of Valency within Carboranedithiol Self-Assembled Monolayers: Molecules Do the Can-Can. *ACS Nano* **2018**, *12*, 2211–2221. https://doi.org/10.1021/acsnano.7b09011.

(11) Kim, J.; Rim, Y. S.; Liu, Y.; Serino, A. C.; Thomas, J. C.; Chen, H.; Yang, Y.; Weiss, P. S. Interface Control in Organic Electronics Using Mixed Monolayers of Carboranethiol Isomers. *Nano Lett.* **2014**, *14*, 2946–2951. https://doi.org/10.1021/nl501081q.

(12) Schwartz, J. J.; Mendoza, A. M.; Wattanatorn, N.; Zhao, Y.; Nguyen, V. T.; Spokoyny, A. M.; Mirkin, C. A.; Baše, T.; Weiss, P. S. Surface Dipole Control of Liquid Crystal Alignment. *J. Am. Chem. Soc.* **2016**, *138*, 5957–5967. https://doi.org/10.1021/jacs.6b02026.

(13) Thomas, J. C.; Schwartz, J. J.; Hohman, J. N.; Claridge, S. A.; Auluck, H. S.; Serino, A. C.; Spokoyny, A. M.; Tran, G.; Kelly, K. F.; Mirkin, C. A.; Gilles, J.; Osher, S. J.; Weiss, P. S. Defect-Tolerant Aligned Dipoles within Two-Dimensional Plastic Lattices. *ACS Nano* **2015**, *9*, 4734–4742. https://doi.org/10.1021/acsnano.5b01329.

(14) Cabarcos, O. M.; Shaporenko, A.; Weidner, T.; Uppili, S.; Dake, L. S.; Zharnikov, M.; Allara, D. L. Physical and Electronic Structure Effects of Embedded Dipoles in Self-Assembled Monolayers: Characterization of Mid-Chain Ester Functionalized Alkanethiols on Au{111}. *J. Phys. Chem. C* **2008**, *112*, 10842–10854. https://doi.org/10.1021/jp801618j.

(15) Abu-Husein, T.; Schuster, S.; Egger, D. A.; Kind, M.; Santowski, T.; Wiesner, A.; Chiechi, R.; Zojer, E.; Terfort, A.; Zharnikov, M. The Effects of Embedded Dipoles in Aromatic Self-Assembled Monolayers. *Adv. Funct. Mater.* **2015**, *25*, 3943–3957. https://doi.org/10.1002/adfm.201500899.

(16) Kang, J. F.; Liao, S.; Jordan, R.; Ulman, A. Mixed Self-Assembled Monolayers of Rigid Biphenyl Thiols: Impact of Solvent and Dipole Moment. *J. Am. Chem. Soc.* **1998**, *120*, 9662–9667. https://doi.org/10.1021/ja981187l.

(17) Kristiansen, K.; Stock, P.; Baimpos, T.; Raman, S.; Harada, J. K.; Israelachvili, J. N.; Valtiner, M. Influence of Molecular Dipole Orientations on Long-Range Exponential Interaction Forces at Hydrophobic Contacts in Aqueous Solutions. *ACS Nano* **2014**, *8*, 10870–10877. https://doi.org/10.1021/nn504687b.

(18) Hohman, J. N.; Claridge, S. A.; Kim, M.; Weiss, P. S. Cage Molecules for Self-Assembly. *Mater. Sci. Eng. R Rep.* **2010**, *70*, 188–208. https://doi.org/10.1016/j.mser.2010.06.008.

(19) Vericat, C.; Vela, M. E.; Benitez, G.; Carro, P.; Salvarezza, R. C. Self-Assembled Monolayers of Thiols and Dithiols on Gold: New Challenges for a Well-Known System. *Chem. Soc. Rev.* **2010**, *39*, 1805. https://doi.org/10.1039/b907301a.

(20) Mete, E.; Yılmaz, A.; Danışman, M. F. A van Der Waals Density Functional Investigation of Carboranethiol Self-Assembled Monolayers on Au(111). *Phys. Chem. Chem. Phys.* **2016**, *18*, 12920–12927. https://doi.org/10.1039/C6CP01485B.

(21) Dickerson, P. N.; Hibberd, A. M.; Oncel, N.; Bernasek, S. L. Hydrogen-Bonding versus van Der Waals Interactions in Self-Assembled Monolayers of Substituted Isophthalic Acids. *Langmuir* **2010**, *26*, 18155–18161. https://doi.org/10.1021/la103494g.

(22) Kim, J. Y.; Jang, W. J.; Kim, H.; Yoon, J. K.; Park, J.; Kahng, S.-J.; Lee, J.; Han, S. Supramolecular Interactions of Anthraquinone Networks on Au{111}: Hydrogen Bonds and van Der Waals Interactions. *Appl. Surf. Sci.* **2013**, *268*, 432–435. https://doi.org/10.1016/j.apsusc.2012.12.117.

(23) Baše, T.; Bastl, Z.; Plzák, Z.; Grygar, T.; Plešek, J.; Carr, M. J.; Malina, V.; Šubrt, J.; Boháček, J.; Večerníková, E.; Kříž, O. Carboranethiol-Modified Gold Surfaces. A Study and Comparison of Modified Cluster and Flat Surfaces. *Langmuir* **2005**, *21*, 7776–7785. https://doi.org/10.1021/la051122d.

(24) Alloway, D. M.; Hofmann, M.; Smith, D. L.; Gruhn, N. E.; Graham, A. L.; Colorado, R.; Wysocki, V. H.; Lee, T. R.; Lee, P. A.; Armstrong, N. R. Interface Dipoles Arising from Self-Assembled Monolayers on Gold: UV−Photoemission Studies of Alkanethiols and Partially Fluorinated Alkanethiols. *J. Phys. Chem. B* **2003**, *107*, 11690–11699. https://doi.org/10.1021/jp034665+.

(25) Evans, S. D.; Goppert-Berarducci, K. E.; Urankar, E.; Gerenser, L. J.; Ulman, A.; Snyder, R. G. Monolayers Having Large In-Plane Dipole Moments:

Characterization of Sulfone-Containing Self-Assembled Monolayers of Alkanethiols on Gold by Fourier Transform Infrared Spectroscopy, x-Ray Photoelectron Spectroscopy and Wetting. *Langmuir* **1991**, *7*, 2700–2709. https://doi.org/10.1021/la00059a050.

(26) Baše, T.; Macháček, J.; Hájková, Z.; Langecker, J.; Kennedy, J. D.; Carr, M. J. Thermal Isomerizations of Monothiolated Carboranes (HS)C 2 B 10 H 11 and the Solid-State Investigation of 9-(HS)-1,2-C 2 B 10 H 11 and 9-(HS)-1,7-C 2 B 10 H 11. *J. Organomet. Chem.* **2015**, *798*, 132–140. https://doi.org/10.1016/j.jorganchem.2015.06.020.

(27) Kwart, H.; Alekman, S. A Cogwheel Effect in the Internal Rotations of Highly Hindered Systems. *J. Am. Chem. Soc.* **1968**, *90*, 4482–4483. https://doi.org/10.1021/ja01018a065.

(28) Lübben, J. F.; Baše, T.; Rupper, P.; Künniger, T.; Macháček, J.; Guimond, S. Tuning the Surface Potential of Ag Surfaces by Chemisorption of Oppositely-Oriented Thiolated Carborane Dipoles. *J. Colloid Interface Sci.* **2011**, *354*, 168–174. https://doi.org/10.1016/j.jcis.2010.10.052.

(29) Baše, T.; Bastl, Z.; Šlouf, M.; Klementová, M.; Šubrt, J.; Vetushka, A.; Ledinský, M.; Fejfar, A.; Macháček, J.; Carr, M. J.; Londesborough, M. G. S. Gold Micrometer Crystals Modified with Carboranethiol Derivatives. *J. Phys. Chem. C* **2008**, *112*, 14446–14455. https://doi.org/10.1021/jp802281s.

(30) Thomas, J. C.; Boldog, I.; Auluck, H. S.; Bereciartua, P. J.; Dušek, M.; Macháček, J.; Bastl, Z.; Weiss, P. S.; Baše, T. Self-Assembled *p*-Carborane Analogue of *p*-Mercaptobenzoic Acid on Au{111}. *Chem. Mater.* **2015**, *27*, 5425–5435. https://doi.org/10.1021/acs.chemmater.5b02263.

(31) Hohman, J. N.; Zhang, P.; Morin, E. I.; Han, P.; Kim, M.; Kurland, A. R.; McClanahan, P. D.; Balema, V. P.; Weiss, P. S. Self-Assembly of Carboranethiol Isomers on Au{111}: Intermolecular Interactions Determined by Molecular Dipole Orientations. *ACS Nano* **2009**, *3*, 527–536. https://doi.org/10.1021/nn800673d.

(32) Langecker, J.; Fejfarová, K.; Dušek, M.; Rentsch, D.; Baše, T. Carbon-Substituted 9,12-Dimercapto-1,2-Dicarba-Closo-Dodecaboranes via a 9,12-Bis(Methoxy-Methylthio)-1,2-Dicarba-Closo-Dodecaborane Precursor. *Polyhedron* **2012**, *45*, 144–151. https://doi.org/10.1016/j.poly.2012.07.067.

(33) Ferris, J. H.; Kushmerick, J. G.; Johnson, J. A.; Yoshikawa Youngquist, M. G.; Kessinger, R. B.; Kingsbury, H. F.; Weiss, P. S. Design, Operation, and Housing of an Ultrastable, Low Temperature, Ultrahigh Vacuum Scanning Tunneling Microscope. *Rev. Sci. Instrum.* **1998**, *69*, 2691–2695. https://doi.org/10.1063/1.1149000.

(34) Melitz, W.; Shen, J.; Kummel, A. C.; Lee, S. Kelvin Probe Force Microscopy and Its Application. *Surf. Sci. Rep.* **2011**, *66*, 1–27. https://doi.org/10.1016/j.surfrep.2010.10.001.

(35) Vetushka, A.; Bernard, L.; Guseva, O.; Bastl, Z.; Plocek, J.; Tomandl, I.; Fejfar, A.; Baše, T.; Schmutz, P. Adsorption of Oriented Carborane Dipoles on a Silver Surface: Adsorption of Oriented Carborane Dipoles on a Silver Surface. *Phys. Status Solidi B* **2016**, *253*, 591–600. https://doi.org/10.1002/pssb.201552446.

(36) Aprà, E.; Bylaska, E. J.; de Jong, W. A.; Govind, N.; Kowalski, K.; Straatsma, T. P.; Valiev, M.; van Dam, H. J. J.; Alexeev, Y.; Anchell, J.; Anisimov, V.; Aquino, F. W.; Atta-Fynn, R.; Autschbach, J.; Bauman, N. P.; Becca, J. C.; Bernholdt, D. E.; Bhaskaran-Nair, K.; Bogatko, S.; Borowski, P.; Boschen, J.; Brabec, J.; Bruner, A.; Cauët, E.; Chen, Y.; Chuev, G. N.; Cramer, C. J.; Daily, J.; Deegan, M. J. O.;

Dunning, T. H.; Dupuis, M.; Dyall, K. G.; Fann, G. I.; Fischer, S. A.; Fonari, A.; Früchtl, H.; Gagliardi, L.; Garza, J.; Gawande, N.; Ghosh, S.; Glaesemann, K.; Götz, A. W.; Hammond, J.; Helms, V.; Hermes, E. D.; Hirao, K.; Hirata, S.; Jacquelin, M.; Jensen, L.; Johnson, B. G.; Jónsson, H.; Kendall, R. A.; Klemm, M.; Kobayashi, R.; Konkov, V.; Krishnamoorthy, S.; Krishnan, M.; Lin, Z.; Lins, R. D.; Littlefield, R. J.; Logsdail, A. J.; Lopata, K.; Ma, W.; Marenich, A. V.; Martin del Campo, J.; Mejia-Rodriguez, D.; Moore, J. E.; Mullin, J. M.; Nakajima, T.; Nascimento, D. R.; Nichols, J. A.; Nichols, P. J.; Nieplocha, J.; Otero-de-la-Roza, A.; Palmer, B.; Panyala, A.; Pirojsirikul, T.; Peng, B.; Peverati, R.; Pittner, J.; Pollack, L.; Richard, R. M.; Sadayappan, P.; Schatz, G. C.; Shelton, W. A.; Silverstein, D. W.; Smith, D. M. A.; Soares, T. A.; Song, D.; Swart, M.; Taylor, H. L.; Thomas, G. S.; Tipparaju, V.; Truhlar, D. G.; Tsemekhman, K.; Van Voorhis, T.; Vázquez-Mayagoitia, Á.; Verma, P.; Villa, O.; Vishnu, A.; Vogiatzis, K. D.; Wang, D.; Weare, J. H.; Williamson, M. J.; Windus, T. L.; Woliński, K.; Wong, A. T.; Wu, Q.; Yang, C.; Yu, Q.; Zacharias, M.; Zhang, Z.; Zhao, Y.; Harrison, R. J. NWChem: Past, Present, and Future. *J. Chem. Phys.* **2020**, *152*, 184102. https://doi.org/10.1063/5.0004997.

(37) Johnson, B. G.; Fisch, M. J. An Implementation of Analytic Second Derivatives of the Gradient-corrected Density Functional Energy. *J. Chem. Phys.* **1994**, *100*, 7429–7442. https://doi.org/10.1063/1.466887.

(38) Adamo, C.; Barone, V. Toward Reliable Density Functional Methods without Adjustable Parameters: The PBE0 Model. *J. Chem. Phys.* **1999**, *110*, 6158–6170. https://doi.org/10.1063/1.478522.

(39) Adamo, C.; Barone, V. Physically Motivated Density Functionals with Improved Performances: The Modified Perdew–Burke–Ernzerhof Model. *J. Chem. Phys.* **2002**, *116*, 5933–5940. https://doi.org/10.1063/1.1458927.

(40) Jensen, F. Unifying General and Segmented Contracted Basis Sets. Segmented Polarization Consistent Basis Sets. *J. Chem. Theory Comput.* **2014**, *10*, 1074–1085. https://doi.org/10.1021/ct401026a.

(41) Yortanlı, M.; Mete, E. Carboxyl- and Amine-Functionalized Carboranethiol SAMs on Au(111): A Dispersion-Corrected Density Functional Theory Study. *Phys. Rev. Mater.* **2020**, *4*, 095002. https://doi.org/10.1103/PhysRevMaterials.4.095002.

(42) Kresse, G.; Furthmüller, J. Efficient Iterative Schemes for *Ab Initio* Total-Energy Calculations Using a Plane-Wave Basis Set. *Phys. Rev. B* **1996**, *54*, 11169–11186. https://doi.org/10.1103/PhysRevB.54.11169.

(43) Kresse, G.; Joubert, D. From Ultrasoft Pseudopotentials to the Projector Augmented-Wave Method. *Phys. Rev. B* **1999**, *59*, 1758–1775. https://doi.org/10.1103/PhysRevB.59.1758.

(44) Blöchl, P. E. Projector Augmented-Wave Method. *Phys. Rev. B* **1994**, *50*, 17953–17979. https://doi.org/10.1103/PhysRevB.50.17953.

(45) Sun, J.; Ruzsinszky, A.; Perdew, J. P. Strongly Constrained and Appropriately Normed Semilocal Density Functional. *Phys. Rev. Lett.* **2015**, *115*, 036402. https://doi.org/10.1103/PhysRevLett.115.036402.

(46) Vydrov, O. A.; Van Voorhis, T. Nonlocal van Der Waals Density Functional: The Simpler the Better. *J. Chem. Phys.* **2010**, *133*, 244103. https://doi.org/10.1063/1.3521275.

(47) Peng, H.; Yang, Z.-H.; Perdew, J. P.; Sun, J. Versatile van Der Waals Density Functional Based on a Meta-Generalized Gradient Approximation. *Phys. Rev. X* **2016**, *6*, 041005. https://doi.org/10.1103/PhysRevX.6.041005.

(48) Yortanlı, M.; Mete, E. Common Surface Structures of Graphene and Au(111): The Effect of Rotational Angle on Adsorption and Electronic Properties. *J. Chem. Phys.* **2019**, *151*, 214701. https://doi.org/10.1063/1.5127099.

(49) Ferrighi, L.; Madsen, G. K. H.; Hammer, B. Self-Consistent Meta-Generalized Gradient Approximation Study of Adsorption of Aromatic Molecules on Noble Metal Surfaces. *J. Chem. Phys.* **2011**, *135*, 084704. https://doi.org/10.1063/1.3624529.

(50) Shepard, S.; Smeu, M. First Principles Study of Graphene on Metals with the SCAN and SCAN+rVV10 Functionals. *J. Chem. Phys.* **2019**, *150*, 154702. https://doi.org/10.1063/1.5046855.

(51) Yeh, I.-C.; Berkowitz, M. L. Ewald Summation for Systems with Slab Geometry. *J. Chem. Phys.* **1999**, *111*, 3155–3162. https://doi.org/10.1063/1.479595.

ORCID

Katherine White: 0000-0001-5050-6024

Erin Avery: 0000-0002-6361-6967

Edison Cummings: 0000-0003-4131-4527

Zixiang Hong: 0000-0001-5259-8559

Aliaksei Vetushka: 0000-0003-3629-2773

Zdeněk Bastl: 0000-0001-6857-4324

Michal Dušek: 0000-0001-9797-2559

Jan Macháček: 0000-0003-4723-0789

Jakub Višňák: 0000-0001-7480-3971

Ersen Mete: 0000-0002-0916-5616

Anastassia N. Alexandrova: 0000-0002-3003-1911

Tomáš Baše: 0000-0003-2533-8705

Paul S. Weiss: 0000-0001-5527-6248

Acknowledgements

TOC graphic